



# Tailored crystalline structure and enhanced impact strength of isotactic polypropylene/high-density polyethylene blend by controlling the printing speed of fused filament fabrication

Jie Leng<sup>1</sup>, Xuanbo Gu<sup>1</sup>, Rui Hong<sup>1</sup>, and Jie Zhang<sup>1,\*</sup>

<sup>1</sup> College of Polymer Science and Engineering, State Key Laboratory of Polymer Materials Engineering, Sichuan University, Chengdu 610065, China

Received: 2 April 2020

Accepted: 19 June 2020

Published online:

26 June 2020

© Springer Science+Business Media, LLC, part of Springer Nature 2020

## ABSTRACT

Fused filament fabrication (FFF) is the most commonly used 3D printing technology. In this work, the isotactic polypropylene/high-density polyethylene blend was used for FFF for the first time. A printing platform with arrays of conical holes was designed to overcome the warpage deformation of product. In order to investigate the influences of shearing force during the nozzle-extrusion process and stretching force during deposition process on the part property, various printing speeds were selected for series of samples. WAXD, SAXS and SEM measurements were used to study the phase morphology and crystalline structure of components. Results reveal that with the increase in printing speed, the PP crystal would deform into shish-kebab structure and PE crystal would deform into epitaxy crystalline structure owing to the strong shearing and stretching forces. These structures improved the impact strength by about 5 times. The printing speed showed slight influence on the thermal behavior. This work confirms the applicability of semicrystalline polymer in FFF technology and gives a deep understanding toward the printing conditions and part property. The obtained results also provide a new method to fabricate high-performance product which will broaden the research field of FFF.

## Introduction

3D printing (3DP), also referred to as additive manufacturing (AM), has become a disruptive technology contrast with conventional polymer processing methods such as injection molding, extrusion

molding and compression molding [1]. Owing to the characteristics of rapid prototyping, mold needless and personalized manufacturing, 3DP has been widely used in automobile industry, rapid molding, architectural engineering, industrial design, aerospace, medical science and many other fields. Among

Address correspondence to E-mail: zhangjie@scu.edu.cn

all the 3DP technologies, i.e., fused filament fabrication (FFF), stereo lithography apparatus (SLA), selective laser sintering (SLS), laminated object manufacturing (LOM), etc. [2–5], FFF is the most commercially and commonly used one. It has many prominent advantages including low cost, portable equipment, no material waste and secure manufacturing environment compared with other 3DP technologies [6, 7]. Since it was first developed by Scott Crump at Stratasys in the early 1990s [8], many efforts have been made to investigate this technology which can be roughly classified into new material development [9, 10], processing parameter optimization [11, 12], equipment development [13, 14], product quality improvement [15, 16] and application field exploration [17, 18]. To our knowledge, material deficiency is the most severe limitation of FFF, as the commercialized polymer materials applied for FFF are mostly restricted to polylactic acid (PLA) and acrylonitrile butadiene styrene (ABS).

The processing procedure of FFF can be described as follows. The thermoplastic filament feedstock is firstly fed into the liquefier by a pair of counter rotating rolls. After melt under the extrinsic heat supply, molten materials are sequentially extruded out of the nozzle with a specific diameter. The solid feedstock plays the role of plunger in the same time. Then, the extruded strands deposit on the printing platform road by road. With the coordination of nozzle and platform movements, the part with any geometry can be finally fabricated under machine instructions. There are two external forces that polymer melt may suffer during printing, that is, the shearing force in the nozzle-extrusion process and the stretching force in the deposition process. As far as we know, some attempts have been made to study the influences of the external forces on the part property. Zhou et al. [19] observed the formation of in situ fibrils and microfibrils in FDM printed PP/PC parts induced during processing. This phenomenon was caused by the orientation of molecular chains under external shearing and stretching forces, and finally resulted in the dramatically improved mechanical properties of FDM parts. Further, they also found that the tensile properties of FDM printed PC/ABS/EMA and PC/ABS/EMA/nano-sodium montmorillonite parts along the deposition direction were higher than that of conventional injection-molded samples [20]. This was attributed to the deposition-induced effect. The deposited materials

underwent external stretching force during the nozzle scanning process, resulting in the orientation of macromolecules which enhanced the tensile properties. In our recent work, the in situ PLA microfibrils were observed in TPU/PLA blend when fabricating parts using the customized FDM printer [21]. Results revealed that these microfibrils mostly formed in the nozzle-extrusion process owing to the shearing force and could be maintained in the final parts. As a result, the tensile properties were largely improved compared with neat TPU samples.

Isotactic polypropylene (iPP) is one of the most commercialized thermoplastics around the world, owing to its comprehensive properties and low cost. However, despite the wide applications in industry, iPP has almost not commercially used in FFF yet. The leading limitation is the severe warpage deformation of printed parts induced by the high degree of crystallinity and shrinkage [22]. As a result, the existing researches mostly focus on the development of printability and part quality of PP [23–29]. But there are extremely rare investigations toward the relationship between crystalline structures and mechanical properties of PP-based FFF parts. High-density polyethylene (HDPE) is also a commonly used thermoplastic, and several researches have been conducted to improve its application in FFF [30–32]. iPP/HDPE blends are widely studied as a polymer blend system [33], especially the investigations about the relationships among the processing conditions, the microstructure of sample and the mechanical properties. Epitaxy crystallization is a well-known crystalline structure of iPP/HDPE blends based on the geometric lattice matching for (010) lattice plane of iPP and (100) lattice plane of PE [34, 35], which can provide excellent properties to products. Some researchers have made attempts to fabricate parts with this structure by traditional polymer processing methods [36–42], but it is still a challenge to largely obtain epitaxy crystalline structure among common samples for industrial applications.

In the present work, iPP/HDPE blend was selected for FFF for the first time. The blend filaments were prepared as feedstock. Considering that both components are semicrystalline polymers with large shrinkage, a self-developed platform which has arrays of conical holes as shown in Fig. 1a was used in order to largely reduce the warpage deformation of printed parts, as well as enhancing the bonding property between the part and platform. During the

printing process, some material of the first layer would flow into the conical holes, solidify and connect the products with the table and decrease the warpage. Because the upper diameter of the holes is as small as 0.46 mm, each immersed material is easy to fracture under suitable external force. So it is easy to remove the printed parts from the self-developed platform without deforming or damaging the morphology. A simple comparison of pure iPP samples printed on the platform with arrays of conical holes and straight holes proves the positive effect of the developed platform as shown in Fig. 1b, and the printed iPP/HDPE sample is shown in Fig. 1c. Because of the fact that the shearing and stretching forces during FFF mainly depend on the printing speed, five different printing speeds were chosen to investigate their influences on the microstructure, thermal behavior and impact property of products. The experimental results indicate that shish-kebab structure of PP phase and epitaxy crystalline structure of PE phase can be found in FFF parts under suitable conditions. Both structures make huge contributions to the enhancement of impact strength.

## Materials and methods

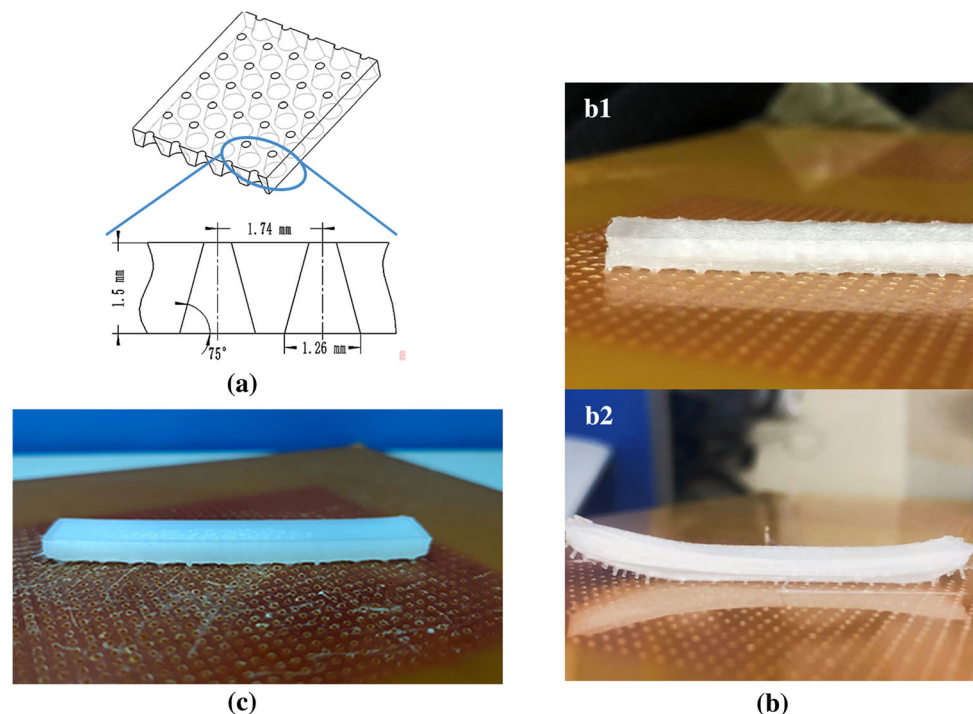
### Materials

Isotactic polypropylene (iPP, trade name T30S), with a melt flow index (MFI) of 2.90 g/10 min (230 °C, 2.16 kg), a  $M_w$  of  $58.7 \times 10^4$ , a molecular weight distribution of 5.2 and a density of  $0.910 \text{ g/cm}^3$ , was purchased from Dushanzi Petroleum Chemical Co., China. High-density polyethylene (HDPE, trade name 5000S), with a melt flow index (MFI) of 1.18 g/10 min (190 °C, 2.16 kg), a  $M_w$  of  $13.2 \times 10^4$ , a molecular weight distribution of 5.6 and a density of  $0.960 \text{ g/cm}^3$ , was supplied by Lanzhou Petroleum Chemical Co., China.

### Sample fabrication

The primary processes of sample fabrication are demonstrated in Fig. 2. HDPE and iPP pellets were oven-dried at 80 °C for 5 h; then, they were melt compounded by a SHJ-25 corotating twin screw extruder (Cheng Meng Plastic Machinery Factory, Nan Jin, China). The mass ratio of iPP to HDPE was 80:20. The screw speed was 120 rpm, and the temperatures from hopper to die were 150, 170, 180, 200, 200, 200, 200, 200, 190 °C, respectively. Extruded polymer melt was cooled by water bath and then cut

**Figure 1** **a** Schematic of the self-developed platform with arrays of conical holes and its geometric dimensions; **b** pure iPP samples printed on the platform with arrays of conical holes (*b1*) and straight holes (*b2*); **c** part of iPP/HDPE blend deposited on the platform.



into granules. After dried at 80 °C for 4 h, the prepared blend pellets were made into filaments suitable for FFF by a FLD-25 single screw extruder (En Beide Machinery co. LTD, Su Zhou, China). The screw speed was 60 rpm, and the temperatures from hopper to die were 160, 190, 190, 190 °C, respectively. The extruded melt was pulled by rolling wheel and frozen through water bath. A laser diameter measuring instrument was used to ensure that the diameter of polymer filaments was precisely controlled at  $1.75 \pm 0.1$  mm by adjusting the pulling speed. Pure iPP and PE filaments were also prepared for measurements in order to investigate the change of crystalline behavior of both components. Then, a commercial desktop 3D printer (HORI Z300) was used to fabricate samples with the prepared blend filaments as feedstock. Impact test samples with dimension of  $60 \times 10 \times 4$  (length  $\times$  width  $\times$  thickness) mm as shown in Fig. 2 were printed. The main processing parameters of FFF process are listed in

Table 1. All samples were printed with a melt infill orientation of 0°, which means that the printing direction was parallel to the length direction of samples. Five different printing speeds were selected including 300, 600, 3000, 6000 and 9000 mm min<sup>-1</sup> for various samples. For simplicity, the final samples were denoted as “PP/PE *x*,” with “*x*” representing the printing speed. To make a comparison with FFF blend samples, pure iPP (named as CPP) and HDPE (named as CPE) samples for impact test were compression molded under the temperature of 200 °C and the pressure of 10 MPa.

### Two-dimensional synchrotron X-ray measurements

The two-dimensional wide-angle X-ray diffraction (2D-WAXD) and two-dimensional small-angle X-ray scattering (2D-SAXS) measurements were taken on the BL16B1 beamline in the Shanghai Synchrotron

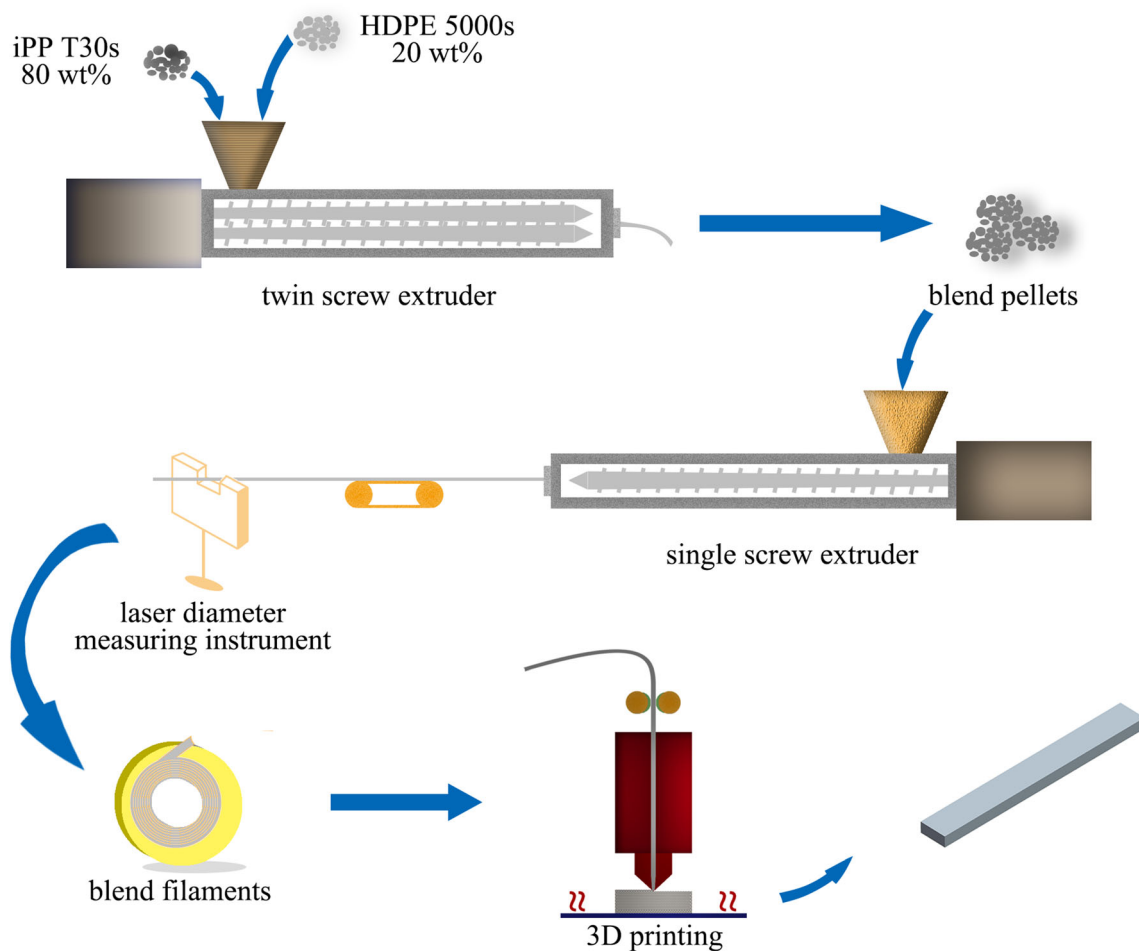


**Figure 2** Schematic diagram of manufacturing procedures from pellets compounding to sample fabrication.

**Table 1** Summary of main printing parameters of the FFF process

Parameters	Values
Nozzle temperature	220 °C
Bed temperature	80 °C
Nozzle diameter	0.8 mm
Layer thickness	0.2 mm
Infill degree	100%
Melt infill orientation	0°
Printing speed	300/600/3000/6000/9000 mm min <sup>-1</sup>

Radiation Facility (SSRF), Shanghai, China. Intermediate zone of each sample was sliced for experiment. The wavelength of X-ray was 0.124 nm, and the rectangular beam with a dimension of  $0.5 \times 2 \text{ mm}^2$  was used. A Pilatus 2 M detector was employed for detection of scattering signals, having a resolution of  $3072 \times 3072$  pixels. The distance from sample to detector was 97.24 mm and 1850 mm for WAXD and SAXS, respectively. The sample was mounted on a three-dimensional elevator platform with its thickness direction parallel to the Y-axis. Finally, Fit-2D, PeakFit and Origin software were used to analyze the data.

Linear WAXD profiles were obtained from circularly integrated intensities of 2D-WAXD patterns. The relative amount of  $\beta$ -crystals  $K_\beta$  in iPP was calculated for each sample using the widely accepted formula proposed by Turner-Jones et al. [43]:

$$K_\beta = \frac{I_\beta(300)}{I_\beta(300) + I_\alpha(110) + I_\alpha(040) + I_\alpha(130)} \quad (1)$$

where  $I_\alpha(110)$ ,  $I_\alpha(040)$  and  $I_\alpha(130)$  are the intensities for  $\alpha$ -form peaks (110), (040) and (130) planes, respectively, while  $I_\beta(300)$  is the intensity of  $\beta$ -form peak (300) in linear WAXD pattern.

Additionally, the orientation degree of lamellar crystals was calculated using the Herman's orientation function [44]. In this method, the crystal orientation was characterized by the average orientation of the normal to the crystal plane with respect to an external reference frame. In this work, the melt infill orientation was taken as the reference direction. For a given  $hkl$  plane, the average orientation, expressed as  $\langle \cos^2 \varphi \rangle_{hkl}$ , was calculated mathematically using the equation:

$$\langle \cos^2 \varphi \rangle_{hkl} = \frac{\int_0^{\pi/2} I(\varphi) \cos^2 \varphi \sin \varphi d\varphi}{\int_0^{\pi/2} I(\varphi) \sin \varphi d\varphi} \quad (2)$$

where  $\varphi$  being the azimuthal angle and  $I(\varphi)$  being the scattered intensity along the angle  $\varphi$ . Herman's orientation function  $f$  was defined as follows:

$$f = \frac{3\langle \cos^2 \varphi \rangle_{hkl} - 1}{2}. \quad (3)$$

Particularly,  $f$  has a value of  $-0.5$  with the normal of the reflection plane being perpendicular to the reference direction ( $\varphi = 90^\circ$ ), a value of  $1$  with the normal of the reflection plane being parallel to the reference direction ( $\varphi = 0^\circ$ ) and a value of  $0$  with the orientation being random. The (040) diffraction rings of iPP in the two-dimensional patterns were chosen for calculating the degree of orientation in this study.

### Scanning electron microscope (SEM)

The morphology of printed samples was observed using scanning electron microscope (FEI Nova Nano SEM, America) with an acceleration voltage of 5 kV. To carefully observe the crystalline morphology, samples were firstly brittle fractured after immersed in liquid nitrogen. Then they were chemically etched in a permanganate etching solution at 50 °C for 8 h, where amorphous phase of both polymers dissolved but crystals remained. The impact fractured surfaces of samples were also investigated. All specimens were gold-sputtered before SEM observation.

### Differential scanning calorimetry

The thermal behavior and crystallinity of each component were measured using a TA-Q200 differential scanning calorimetry instrument. All measurements were taken under nitrogen atmosphere. Specimens of around 4 mg were cut from samples, placed in a sealed aluminum pan and then heated from 80 to 200 °C at a heating rate of 10 °C min<sup>-1</sup>. The crystallinity  $X_c$  of component  $i$  in the blend was calculated by the following equation [45]:

$$X_c = \frac{\Delta H_i}{\varphi_i \Delta H_i^m} \quad (4)$$

where  $\Delta H_i$  is the enthalpy of fusion of component  $i$ , directly obtained from DSC results, and  $\varphi_i$  is the mass fraction of component  $i$  in the blend. The fusion

enthalpy  $\Delta H_i^m$  of fully crystalline polymer is 207 and 293 J g<sup>-1</sup> for iPP and HDPE, respectively.

### Measurement of impact strength

The notched Izod impact strength of the specimens was measured with a XJUD-5.5 Izod machine (Jinjian Testing Instrument co. LTD, China) at room temperature according to ASTM D256-04. Before the test, a 45° V-shaped notch (depth 2 mm) was made. For each sample, at least five specimens were used and the values of all mechanical parameters were calculated as averages.

## Results and discussion

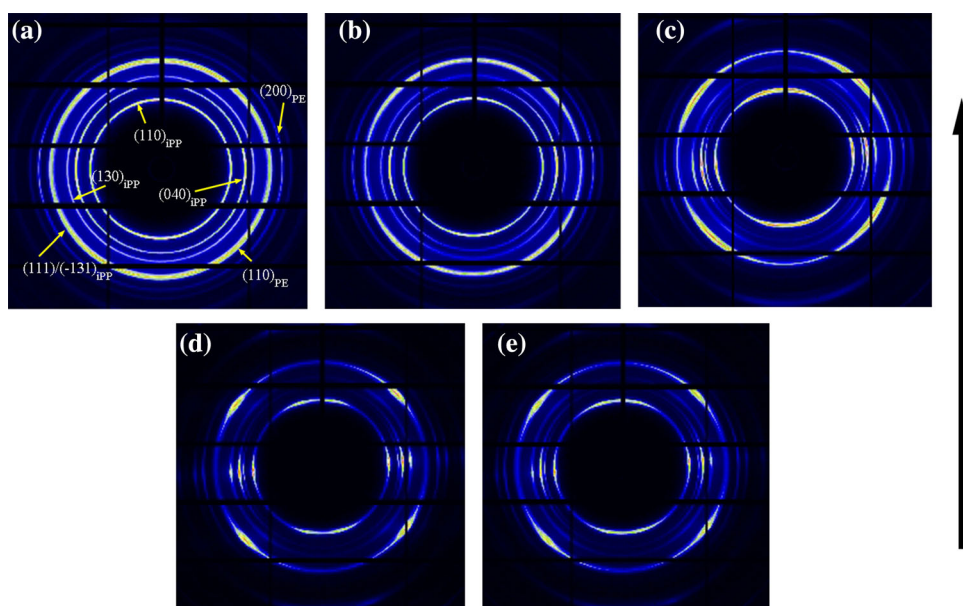
### Two-dimensional wide-angle X-ray diffraction

Figure 3 shows the 2D-WAXD patterns obtained at the intermediate zones of various samples, which are used to investigate the crystalline status of the blend. From inner to outward, the reflection circles or arcs originate from (110), (040), (130), (111) and (−131) planes of  $\alpha$  modification of iPP and (110), (200) planes of orthorhombic crystallites of HDPE. Specially, for iPP/HDPE blends, the reflections of (111) and (−131) planes of iPP are overlapped with (110) plane of HDPE as a result of their similar diffraction angles. When the printing speed is as low as 300 mm min<sup>-1</sup>,

it can be clearly seen in Fig. 3a that all reflections of iPP and HDPE are unabridged and equally distributed circles, indicating isotropic crystallization of both components [36]. Slight difference occurs when the printing speed increases to 600 mm min<sup>-1</sup>. However, strong arc-like diffraction signals appear for samples with printing speed larger than 3000 mm min<sup>-1</sup>, as shown in Fig. 3c–e. Note that the strong reflections of iPP ( $hk0$ ) planes at the equator direction indicate that the  $c$ -axis of iPP lamellae are preferentially oriented along the melt infill orientation. That is to say, the molecular chains show strong tendency to orient parallel to the melt infill orientation with high orientation degree. For the (110), (111) and (−131) planes of iPP, four reflection arcs symmetrically emerged around the meridian, which is identical to Liu's [46] results. Moreover, an additional (300) lattice plane appears in samples (b–e) corresponding to the reflection of  $\beta$ -crystals of iPP.

To further investigate the crystalline structure and orientation degree of blend, the linear WAXD curves of various samples are presented in Fig. 4 after circularly integrating the intensities of 2D-WAXD patterns. The reflection peaks represent different lattice planes of iPP and HDPE, with the increase of 2-theta angle. It is obvious that diffraction peaks of (300) lattice plane of  $\beta$ -crystal exist in all samples except for PP/PE 300, which possesses the lowest printing speed. The orientation degree and relative content of  $\beta$ -crystals of iPP are calculated and plotted in Fig. 5 using the methods mentioned in “Two-dimensional

**Figure 3** 2D-WAXD patterns at the intermediate zones of different samples: **a** PP/PE 300; **b** PP/PE 600; **c** PP/PE 3000; **d** PP/PE 6000; **e** PP/PE 9000. The melt infill orientation is perpendicular indicating by a black arrow.



synchrotron X-ray measurements” section. From Fig. 5, we can see that the orientation degree of iPP increases sharply with the increase in printing speed at first, i.e., from 0.5045 for PP/PE 300 to 0.9311 for PP/PE 3000. But it then changes slightly to 0.9512 for PP/PE 6000 and decreases to 0.8974 for PP/PE 9000. This is caused by the fact that during the printing process, when polymer melt is extruded out of nozzle and deposits on the platform, iPP molecular chains are subjected to the shearing force in the nozzle and stretching force successively, which will cause the molecular chains to orient along the nozzle scanning direction. The decrease in orientation degree for PP/PE 9000 may be attributed to the slower cooling rate under extremely high printing speed. These oriented molecular chains then induced the generation of a few  $\alpha$ -row nuclei, and the surface of the row structures provided nucleation sites for  $\beta$ -crystal growth. The content of  $\beta$ -crystals remarkably depends on the shearing and stretching force controlled by printing speed. As can be seen in Fig. 5, the relative content of  $\beta$ -crystals  $K_\beta$  also increases with the increase in printing speed at first, i.e., from 0 for PP/PE 300 to 6.56% for PP/PE 3000. However, when the printing speed increases further to 6000 mm min<sup>-1</sup>, the  $K_\beta$  decreases to 4.92% because of the formation of extremely high-oriented structures which have an adverse effect for  $\beta$ -crystal growth [47, 48]. The  $K_\beta$  then increases to 5.92% for PP/PE 9000 with the decrease in orientation degree. Moreover, note that when the nozzle temperature is 220 °C and the heated bed temperature is 80 °C, the sample printed

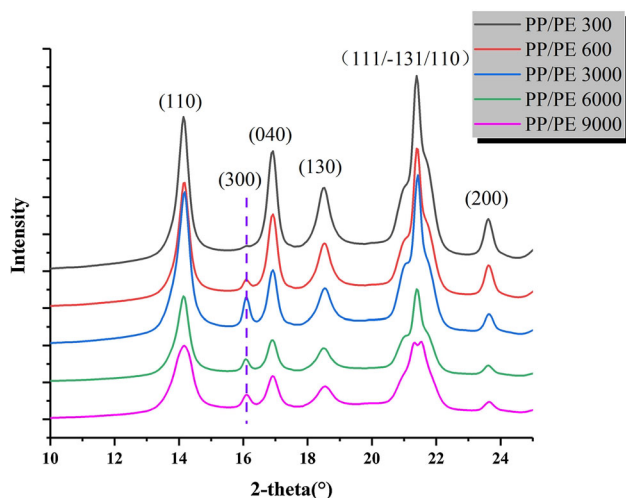


**Figure 4** 1D-WAXD curves of various samples obtained from circularly integrating intensities of 2D-WAXD patterns.

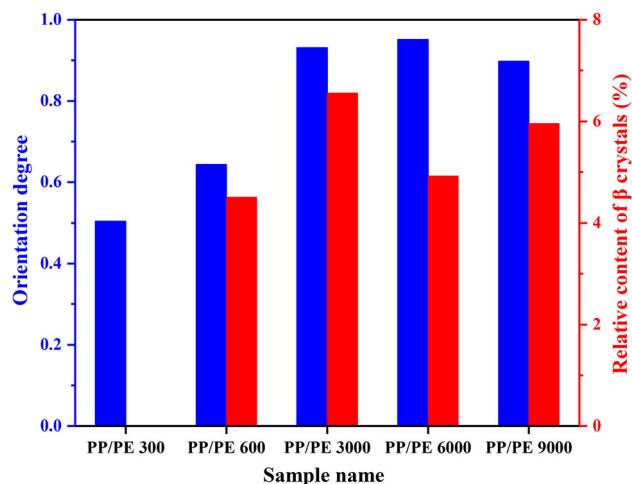


**Figure 5** Orientation degree and relative content of  $\beta$ -crystals of iPP in various samples.

on the platform should have a relative long duration at the temperature window of 100 ~ 130 °C, which is beneficial for the  $\beta$ -crystal growth [48].

### Two-dimensional small-angle X-ray scattering

2D-SAXS measurement was used to further investigate the crystalline morphology of components with the obtained results shown in Fig. 6. The 2D scattering patterns of various samples are labeled (a–e), for samples with printing speed of 300, 600, 3000, 6000 and 9000 mm min<sup>-1</sup>, respectively. The corresponding azimuthal scan of the 2D-SAXS patterns is also shown in Fig. 7. Note that the melt infill orientation is the vertical direction for all samples. It can be clearly seen in Fig. 6a and b that for PP/PE 300 and PP/PE 600 samples, reflections only occur at directions 0° and 180°, which can be identified by the azimuthal angles in Fig. 7. This can be mainly ascribed to the inferior orientation arrangement of iPP lamellae. As discussed above, the orientation degree of iPP is 0.5045 and 0.6436 for PP/PE 300 and PP/PE 600, respectively. The orientation degree of PE seems also extremely low. However, it changes dramatically when the printing speed increases to 3000 mm·min<sup>-1</sup>. As can be seen in Fig. 6c–e, iPP exhibits typical shish-kebab structures for all samples. Correspondingly, there are four peaks in azimuthal scan curves which locate at 0°, 180°, 90° and –90°. Normally, azimuthal angles distribute at 0° and 180° refer to the signal of the shish, whereas

**Figure 6** 2D-SAXS patterns at the intermediate zones of various samples: **a** PP/PE 300; **b** PP/PE 600; **c** PP/PE 3000; **d** PP/PE 6000; **e** PP/PE 9000. The melt inflill orientation is perpendicular for all samples.

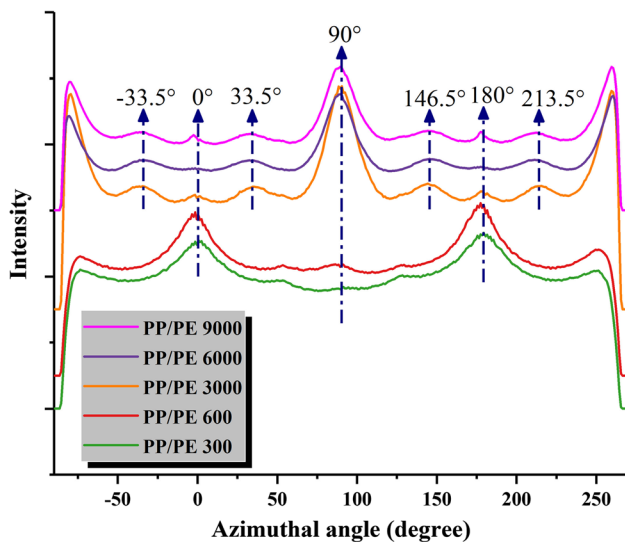
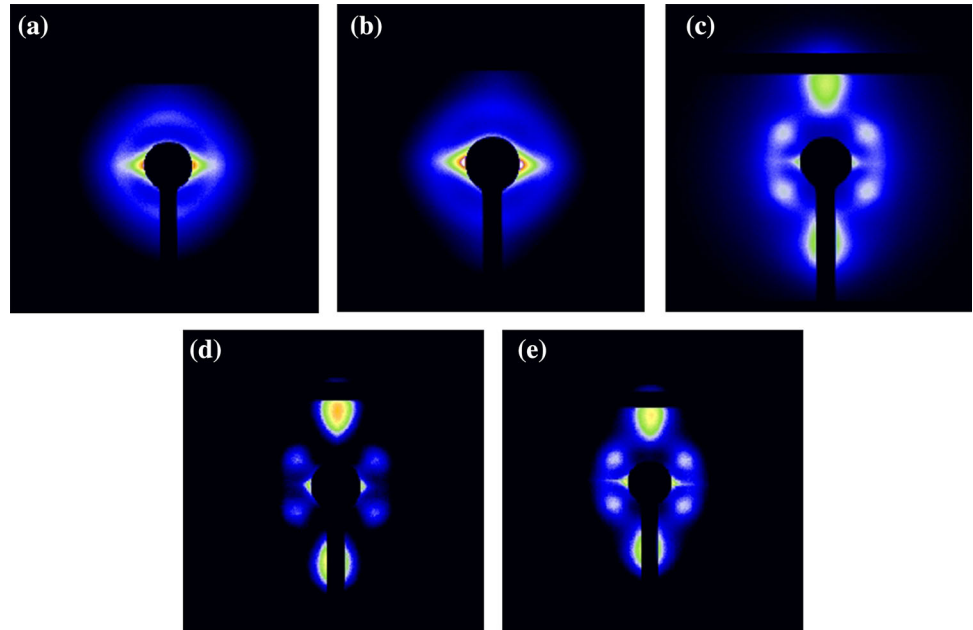


**Figure 7** Azimuthal scan of the 2D-SAXS patterns of various samples.

azimuthal angles distribute at  $-90^\circ$  and  $+90^\circ$  refer to the signal of the kebab. Moreover, the scattering intensities at  $90^\circ$  and  $-90^\circ$  for samples with printing speed of 3000, 6000 and  $9000 \text{ mm min}^{-1}$  are much stronger than that at  $0^\circ$  and  $180^\circ$ . This result is almost opposite to samples printed with 300 and  $600 \text{ mm min}^{-1}$ , indicating the formation of highly oriented shish-kebab structures caused by the increasing printing speed. Similar results were observed by Shmueli et al. [49]. They designed a novel apparatus which can measure the SAXS, MAXS

and WAXS spectra of printed iPP structures with micrometer resolution in situ during materials extrusion 3D printing and found that the high shear of the nozzle resulted in the formation of shish-kebab structures in the iPP strands after extrusion. They also observed that the shish-kebab structures formed initially at the surface of the deposited strands and propagated inward toward the core. However, for PP/PE 3000, PP/PE 6000 and PP/PE 9000 samples, besides the strong scattering signals which belong to iPP oriented structures, there are other four scattering signals uniformly distribute apart about  $\pm 33.5^\circ$  from the equator direction separately. Compared with the other studies concentrating on the crystalline morphology of iPP/PE blends [34, 37, 38], these scattering spots indicate the special epitaxial growth of PE lamellae on the oriented iPP lamellae, that is, the signals of epitaxy crystallization behaviors. It can be seen more evidently in Fig. 7 that there are four additional peaks at  $-33.5^\circ$ ,  $33.5^\circ$ ,  $146.5^\circ$  and  $213.5^\circ$  in the upper three curves. Their relatively weak intensity should be attributed to the minor mass ratio of PE component, i.e., 20% in this work. The further observation of the peculiar epitaxy crystallization and the formation mechanism will be discussed in the next section.



## Crystalline morphology

The SEM micrographs of the cryo-fractured cross section of PP/PE 300, PP/PE 3000 and PP/PE 9000 before chemical etching are shown in Fig. 8. Several deposited layers are contained in each micrograph as the layer thickness was set as 0.2 mm in this work. It can be clearly seen from these figures that all the samples are fully filled, showing dense cross sections without any voids or cracks. The bonding interfaces of adjacent layers and adjacent strands are completely invisible for all samples except for the interfaces of adjacent layers of PP/PE 9000 which are slightly discernible. These results indicate that the deposited material has good interfacial reaction under the printing conditions, which are supposed to promote the mechanical strength.

Figure 9 illustrates the SEM micrographs at the intermediate zones of samples with different printing speeds. To intuitively understand the relationship between morphology and SAXS reflections, the relevant 2D-SAXS pattern of each sample is inserted at the corner. It is notable that the melt infill orientation is horizontal for SEM images but is vertical for SAXS patterns. After the samples have been chemically etched in a permanganate etching solution, one can clearly distinguish the iPP and PE crystals in the SEM images according to their discrepant mass ratio. The dark areas in the photographs refer to iPP matrix, whereas the relatively white regions represent PE phase. It can be clearly seen that for PP/PE 300 and PP/PE 600 samples, where the printing speeds are slow, the iPP crystals demonstrate isotropic growth in the whole region without any orientation structures can be seen. Additionally, the minor PE phase is uniformly distributed in iPP matrix with randomly arranged crystal lamellae. It is known that PE phase is incompatible with PP phase so they usually form a

so-called immiscible system. It can be inferred that when printing with such slow speeds, both PE and iPP molecular chains suffer relatively weak shearing force and stretching force in the extrusion and deposition processes, respectively, leading the isotropic growth of both crystals. These results are identical with the relevant SAXS signals.

However, things change dramatically when the printing speed increases to  $3000 \text{ mm min}^{-1}$ . As can be seen in Fig. 9c–e, iPP phase in these samples exhibits typical oriented crystalline morphology in the whole region, with its lamellae aligns almost vertical to the melt infill orientation. These oriented crystals refer to shish-kebab structures formed during the extrusion and deposition processes under high printing speed, as certified by the inserted SAXS patterns and the WAXD results discussed above. Moreover, the dispersed PE phase mainly formed inclined lamellae in these samples. This specific crystalline structure also exists in the whole region. With the evidence of XRD results, this special phenomenon should be the typical epitaxy crystalline morphology in PP/PE blends, which has been adequately presented in previous studies [34–38, 50]. The epitaxy crystallization is formed based on the geometric lattice matching for the (100) lattice plane of PE and the (010) lattice plane of iPP as PE chains can exactly fit into the valleys formed by the methyl groups of iPP [51]. It is worth noting that the average length of the epitaxy crystalline structures decreases with the increase in printing speed, and PP/PE 3000 sample possesses the longest epitaxy crystalline structure. The unduly high printing speed such as 6000 and  $9000 \text{ mm min}^{-1}$  would cause a high stretching force during deposition and pull apart the dispersed PE phase. Considering the fact that the formation of highly oriented iPP matrix is the basis of the epitaxy crystallization, the formation mechanism

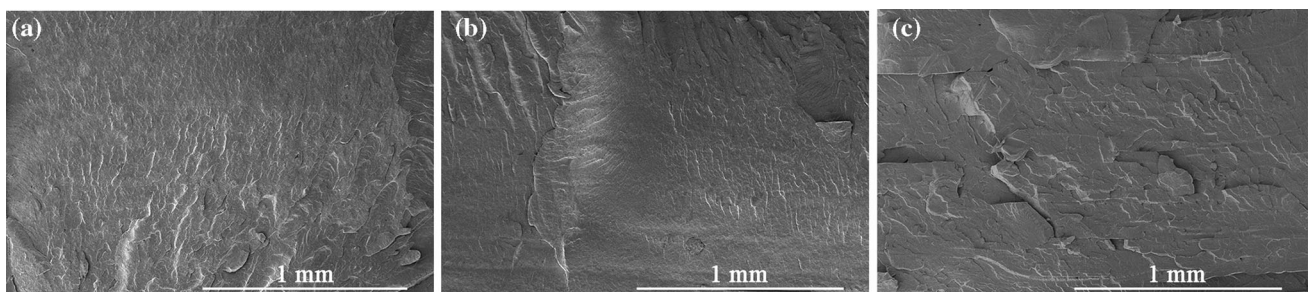


**Figure 8** Scanning electron microscopy micrographs of the cryo-fractured cross section for **a** PP/PE 300; **b** PP/PE 3000 and **c** PP/PE 9000.

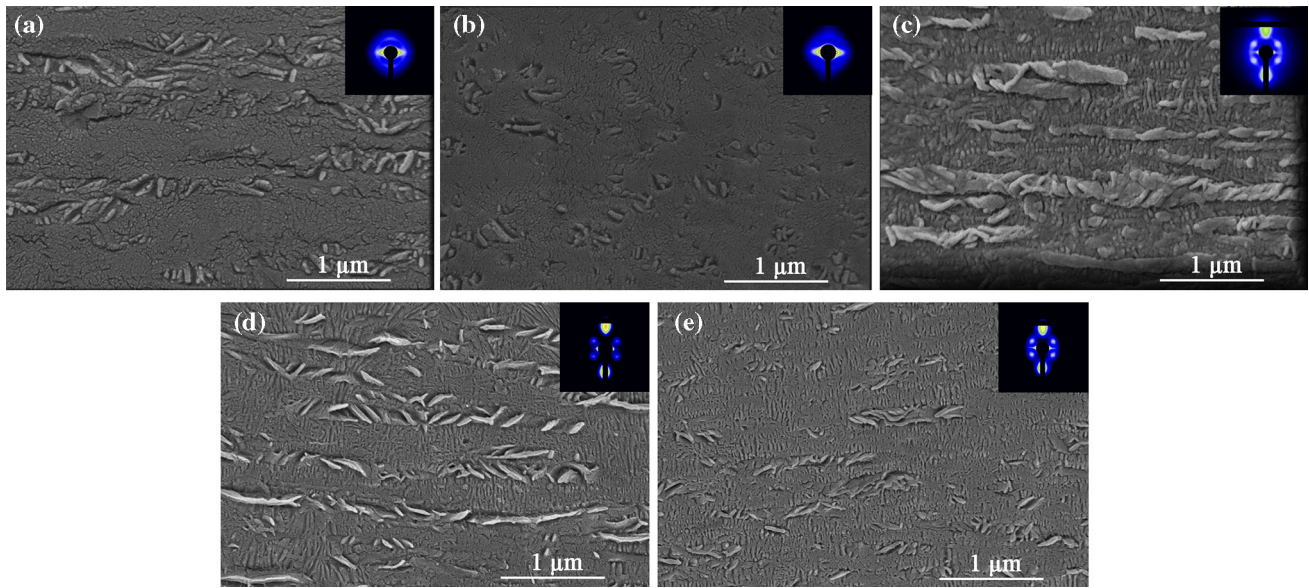


**Figure 9** Scanning electron microscopy micrographs at the intermediate zones of different samples: **a** PP/PE 300; **b** PP/PE 600; **c** PP/PE 3000; **d** PP/PE 6000; **e** PP/PE 9000. The relevant

of epitaxy morphology in the present work can be explained as follows. During 3D printing, the polymer melt undergoes external shearing force in the nozzle-extrusion process and stretching force in the strand-deposition process. Both forces are mainly dependent on the printing speed, and they contribute a lot to the orientation of molecular chains [19, 20, 52]. When the printing speed is slow, both forces are insignificant and iPP matrix and PE phase distribute randomly. However, high shearing and stretching forces induced by the increased printing speed can promote the molecular chains orient along the melt infill orientation. iPP chains form highly oriented shish-kebab structures in this case which can be adequately remained after freezing, but the relatively low molecular weight of HDPE and relatively high molding temperature ensure PE chains to fully relax and recrystallize onto the oriented iPP lamellae. Finally, the peculiar epitaxy crystallization morphology appears in the printed part.

### Thermal behavior

The DSC melting curves of various samples are demonstrated in Fig. 10. Notably, the PP/PE specimens were cut from printed samples, while pure PP and PE specimens were cut from their filaments. The corresponding melting points and crystallinities are also calculated from the DSC curves and presented in

Table 2. There are two melting peaks for PP/PE blend, where the lower one refers to PE phase and the higher one refers to PP phase. It can be clearly seen from Table 2 that the melting points and crystallinities of both iPP and PE phases exhibit slight variations with the change of printing speed. Moreover, when compared with neat polymer, the melting point and crystallinity of PP phase in different printed samples also remain almost the same. But they

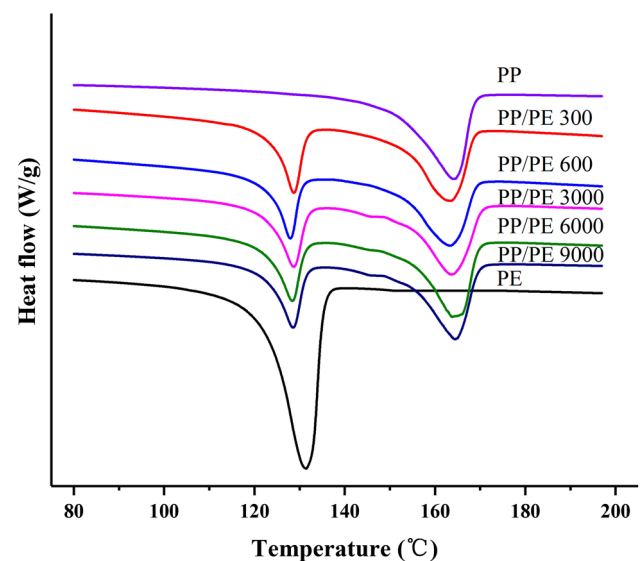


**Figure 10** DSC melting curves of various samples. Neat PP and PE samples are cut from their filaments.

change apparently for the minor PE phase. The melting point of PE phase decreases about 3 °C from neat PE to printed samples with various printing speeds, while the crystallinity of PE phase increases from 43 to about 50%. It is confirmed that the sample temperature and shear flow have significant influences on the crystallization of semicrystalline polymers during FFF [53–55]. Considering the processing conditions in this work mentioned above, it can be assumed that the crystalline behavior of PP phase can be hardly affected but PE molecular chains show strong opportunity for relaxation and recrystallization. So PE phase tends to crystallize more completely, causing the final changes of its thermal property.

### Mechanical property

The impact strength of various samples is presented in Fig. 11a. The impact strength of CPP and CPE is 3.42 kJ m<sup>-2</sup> and 13.38 kJ m<sup>-2</sup>, respectively. The higher impact strength of printed iPP/HDPE blends compared with pure iPP can be partially attributed to the better toughness of HDPE component. It can be obviously seen that samples with high printing speed of 3000 mm min<sup>-1</sup> have significantly higher impact strength than samples with low printing speed. It is worth noting that samples fabricated with high printing speed cannot fully rupture during impact test, which is opposite to slowly printed samples. The typical sample images of PP/PE 300 and PP/PE 3000 after impact test are shown in Fig. 11b. The impact strength of PP/PE 300 is the lowest for FFF samples, which is 11.07 kJ m<sup>-2</sup>, and it increases to 14.19 kJ m<sup>-2</sup> for PP/PE 600. This improvement may be ascribed to the higher  $\beta$ -crystal content of PP/PE

600, as  $\beta$ -crystal is confirmed with a relatively better toughness. However, when the printing speed increases to 3000 mm min<sup>-1</sup>, the impact strength increases dramatically to 55 kJ m<sup>-2</sup> which is about 5 times higher than that of PP/PE 300 sample. The impact strength of PP/PE 6000 and PP/PE 9000 decreases to about 41 kJ m<sup>-2</sup>, but is still much higher than PP/PE 300 and PP/PE 600. The unexpected improvement can be explained in two aspects. On the one hand, the highly oriented shish-kebab structure of iPP phase induced by high printing speed can largely enhance the impact strength. On the other hand, the epitaxy crystalline structure of PE phase formed in the samples with high printing speed will further improve the impact strength [36–38, 50]. The greatest impact toughness appears in PP/PE 3000 sample rather than samples with higher printing speed such as 6000 and 9000 mm min<sup>-1</sup>. This should be attributed to the relatively shorter epitaxy crystalline structure of PE phase caused by the excessively high printing speed, as can be clearly seen in Fig. 9.

Meanwhile, the impact fractured surfaces of PP/PE 300 and PP/PE 3000 samples are also observed to better understand the variation of impact strength, and the SEM images are shown in Fig. 11b. It can be seen that the fracture surface of PP/PE 300 sample is rough and rugged, and relatively dense without gaps and voids in the whole range. However, things change for PP/PE 3000 sample. Typical layered structure can be clearly seen on the fracture surface, with the thickness of each layer being 0.2 mm. Apparent gaps exist among adjacent layers on the cross section. In addition, some cracks also appear on the fracture surface of each layer, making it much more rough. It can be inferred from the above results that in order to sustain the energy loading during impact test, the gaps between adjacent layers and cracks on the fracture surface form rapidly to propagate external force, resulting in the extremely higher impact strength compared with that of PP/PE 300 sample.

### Application in 3D printing

In order to verify the printability and part quality of the prepared PP/PE blend, some products including a hollow cube, a multihole cube, a gear and a hexagon ring were printed with their images shown in Fig. 12. The original model shape of each product is

**Table 2** Summary of melting points and crystallinities of various samples calculated from the relative DSC melting curves

Sample	PP phase		PE phase	
	$T_m$ (°C)	$X_c$ (%)	$T_m$ (°C)	$X_c$ (%)
PP	164.30	34.54	–	–
PP/PE 300	163.38	35.08	128.63	50.39
PP/PE 600	163.27	34.71	127.95	50.45
PP/PE 3000	163.67	34.83	128.62	50.58
PP/PE 6000	163.82	34.57	128.38	49.88
PP/PE 9000	164.44	34.71	128.53	51.09
PE	–	–	131.13	43.00

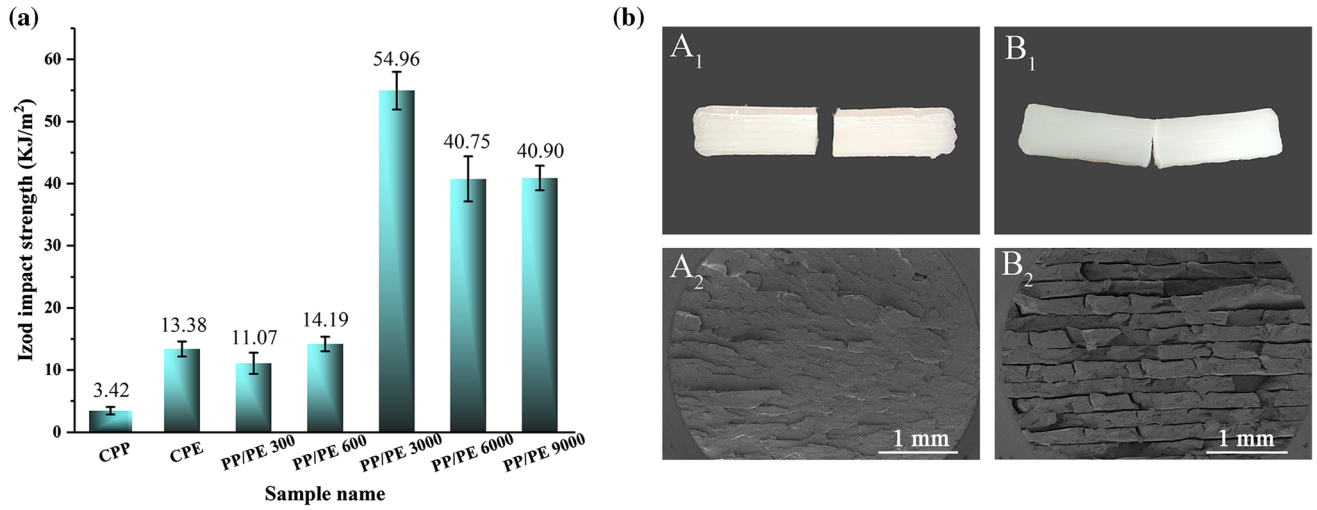
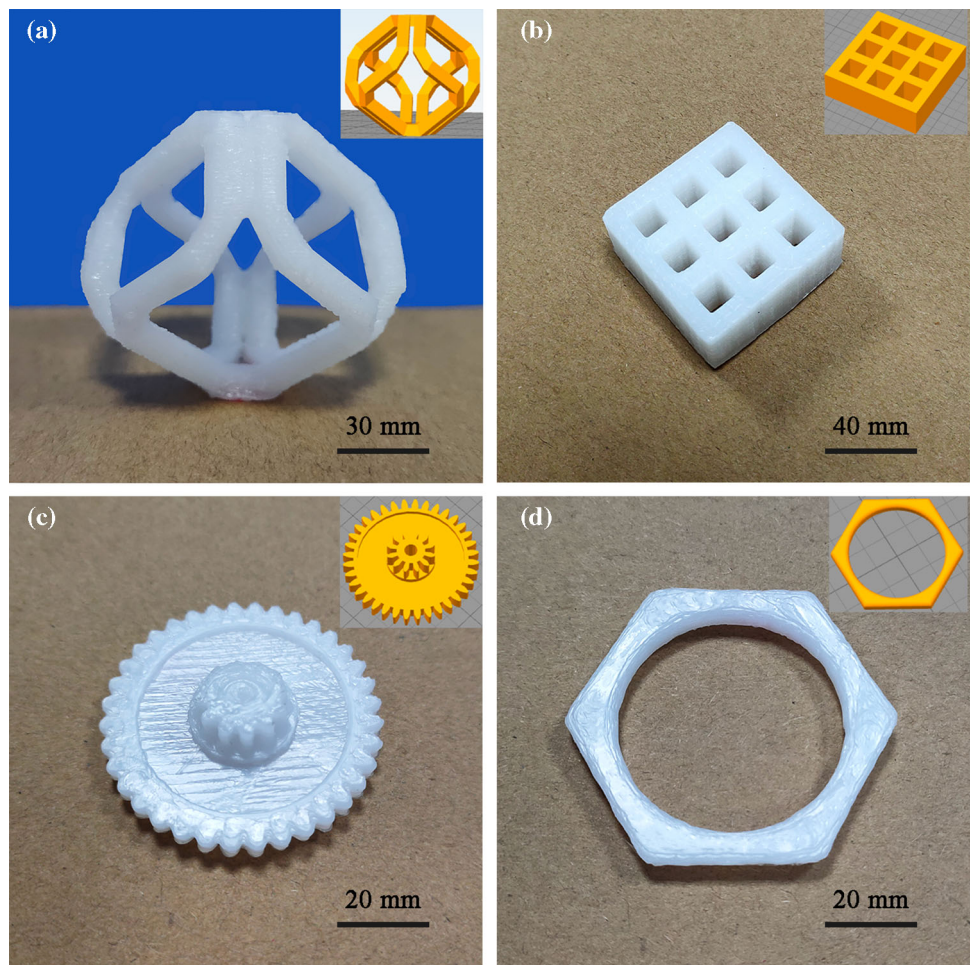


**Figure 11** a Izod impact strength of various samples; b Sample images after impact test and scanning electron microscopy micrographs of their fracture surfaces. “A” refers to PP/PE 300 sample, and “B” refers to PP/PE 3000 sample.

**Figure 12** Illustration of some parts fabricated using the prepared PP/PE blend filaments, including a hollow cube, a multihole cube, a gear and a hexagon ring, with the original model shape of each product inserted in the upper right corner. The printing parameters are shown in Table 1 with a printing speed of 3000 mm min<sup>-1</sup>.



inserted in the upper right corner of each image. The printing parameters used to fabricate these parts are the same as those listed in Table 1, and a printing speed of  $3000 \text{ mm min}^{-1}$  was selected. It can be seen that parts with various geometric structures can be perfectly fabricated with smooth printing procedure and good shape retention. The surface finish of all parts is also worthy to be affirmed. It can be inferred that this developed blend filament is applicative in 3D printing technology, which enriches the material field. Meanwhile, it is also effective to fabricate parts with high mechanical performance by adjusting the printing parameters as discussed above.

## Conclusion

This work creatively selected iPP/HDPE blend as raw material for FFF. The blend filaments were prepared, and products with good shape retention were successfully fabricated using the self-developed printing platform. The variation of phase morphology, thermal behavior and impact strength for samples with different printing speeds is discussed. Due to the strong shearing force in the nozzle-extrusion process and stretching force in the deposition process, the PP phase can deform into highly oriented shish-kebab structure and PE phase can form peculiar epitaxy crystalline structure at a relatively high printing speed. The oriented molecular chains are parallel to the nozzle scanning direction. These structures are confirmed to effectively improve the impact toughness. The thermal behaviors of both components barely change with the variation of printing speed. As semicrystal polymer like iPP has been rarely applied in FFF and the researches about crystal structure are also limited, this work not only extends the material field of FFF but also provides a better understanding of the relationship between the printing conditions and phase morphology.

## Acknowledgements

This work was financially supported by the National Natural Science Foundation of China (51433006) and the open project of Key Laboratory for Precision and Non-Traditional Machining Technology, Dalian University of Technology (JMTZ201702). The authors also want to express their sincere thanks to the

Shanghai Synchrotron Radiation Facility (SSRF, Shanghai, China) for support on WAXD and SAXS measurements.

## Authors contributions

JL contributed to conception, experimental design, carrying out measurements and manuscript composition, XG contributed to conception and carrying out measurements, RH contributed to carrying out measurements, and JZ contributed to conception, experimental design and manuscript composition.

## Funding

This study was funded by the National Natural Science Foundation of China (Grant Number 51433006) and the open project of Key Laboratory for Precision and Non-Traditional Machining Technology, Dalian University of Technology (Grant number JMTZ201702).

## Data and code availability

No data or code is available to readers in this submitted work.

## Compliance with ethical standards

**Conflict of interest** The authors declare that they have no conflict of interest.

## References

- [1] Valino AD, Dizon JRC, Espera AH, Chen QY, Messman J, Advincula RC (2019) Advances in 3D printing of thermoplastic polymer composites and nanocomposites. *Prog Polym Sci* 98:101162–101219. <https://doi.org/10.1016/j.propolymsci.2019.101162>
- [2] Pham DT, Gault RS (1998) A comparison of rapid prototyping technologies. *Int J Mach Tools Manuf* 38(10–11):1257–1287. [https://doi.org/10.1016/s0890-6955\(97\)00137-5](https://doi.org/10.1016/s0890-6955(97)00137-5)
- [3] Nannan G, Leu MC (2013) Additive manufacturing: technology, applications and research needs. *Front Mech Eng* 8(3):215–243. <https://doi.org/10.1007/s11465-013-0248-8>
- [4] Wu J, Xu X, Zhao Z, Wang M, Zhang J (2018) Study in performance and morphology of polyamide 12 produced by

- selective laser sintering technology. *Rapid Prototyp J* 24(5):813–820. <https://doi.org/10.1108/rpj-01-2017-0010>
- [5] Hong R, Zhao Z, Leng J, Wu J, Zhang J (2019) Two-step approach based on selective laser sintering for high performance carbon black/polyamide 12 composite with 3D segregated conductive network. *Compos Part B Eng* 176:107214 (11 pages). <https://doi.org/10.1016/j.compositesb.2019.107214>
- [6] Turner BN, Strong R, Gold SA (2014) A review of melt extrusion additive manufacturing processes: I. Process design and modeling. *Rapid Prototyp J* 20(3):192–204. <https://doi.org/10.1108/rpj-01-2013-0012>
- [7] Wang X, Jiang M, Zhou Z, Gou J, Hui D (2017) 3D printing of polymer matrix composites: a review and prospective. *Compos Part B Eng* 110:442–458. <https://doi.org/10.1016/j.compositesb.2016.11.034>
- [8] Huang SH, Liu P, Mokasdar A, Hou L (2013) Additive manufacturing and its societal impact: a literature review. *Int J Adv Manuf Technol* 67(5–8):1191–1203. <https://doi.org/10.1007/s00170-012-4558-5>
- [9] Wu J, Chen N, Bai F, Wang Q (2018) Preparation of poly(vinyl alcohol)/poly(lactic acid)/hydroxyapatite bioactive nanocomposites for fused deposition modeling. *Polym Compos* 39:E508–E518. <https://doi.org/10.1002/pc.24642>
- [10] Rahim T, Abdullah AM, Akil HM (2019) Recent developments in fused deposition modeling-based 3D printing of polymers and their composites. *Polym Rev* 59(4):589–624. <https://doi.org/10.1080/15583724.2019.1597883>
- [11] Aa A, Qattawi A (2018) Investigating the effect of fused deposition modeling processing parameters using Taguchi design of experiment method. *J Manuf Process* 36:164–174. <https://doi.org/10.1016/j.jmapro.2018.09.025>
- [12] Mohan N, Senthil P, Vinodh S, Jayanth N (2017) A review on composite materials and process parameters optimisation for the fused deposition modelling process. *Virtual Phys Prototyp* 12(1):47–59. <https://doi.org/10.1080/17452759.2016.1274490>
- [13] Schmidt L, Schrickler K, Bergmann JP, Hussenoeder F, Eiber M (2019) Characterization of a granulate-based strand deposition process in the FLM-method for definition of material-dependent process strategies. *Rapid Prototyp J* 25(1):104–116. <https://doi.org/10.1108/rpj-09-2017-0186>
- [14] Leng J, Wu J, Chen N, Xu X, Zhang J (2019) The development of a conical screw-based extrusion deposition system and its application in fused deposition modeling with thermoplastic polyurethane. *Rapid Prototyp J* 26(2):409–417. <https://doi.org/10.1108/rpj-05-2019-0139>
- [15] Boschetto A, Bottini L (2014) Accuracy prediction in fused deposition modeling. *Int J Adv Manuf Technol* 73(5–8):913–928. <https://doi.org/10.1007/s00170-014-5886-4>
- [16] Boschetto A, Giordano V, Veniali F (2013) Surface roughness prediction in fused deposition modelling by neural networks. *Int J Adv Manuf Technol* 67(9–12):2727–2742. <https://doi.org/10.1007/s00170-012-4687-x>
- [17] McCullough EJ, Yadavalli VK (2013) Surface modification of fused deposition modeling ABS to enable rapid prototyping of biomedical microdevices. *J Mater Process Technol* 213(6):947–954. <https://doi.org/10.1016/j.jmatprotec.2012.12.015>
- [18] Martens T, Mears L, Dotson M, Graham M, Sanger P (2011) Use of fused deposition modeling of polyphenylsulfone for centrifugal casting of polyurethane: material, surface, and process considerations. *J Manuf Sci Eng Trans ASME* 133(5):051003 (10 pages). <https://doi.org/10.1115/1.4004848>
- [19] Zhou Y-G, Su B, Turng L-s (2017) Deposition-induced effects of isotactic polypropylene and polycarbonate composites during fused deposition modeling. *Rapid Prototyp J* 23(5):869–880. <https://doi.org/10.1108/rpj-12-2015-0189>
- [20] Zhou Y-G, Zou J-R, Wu H-H, Xu B-P (2020) Balance between bonding and deposition during fused deposition modeling of polycarbonate and acrylonitrile-butadiene-styrene composites. *Polym Compos* 41(1):60–72. <https://doi.org/10.1002/pc.25345>
- [21] Leng J, Wu J, Zhang J (2019) Preparation of thermoplastic polyurethane parts reinforced with in situ polylactic acid microfibers during fused deposition modeling: the influences of deposition-induced effects. *Ind Eng Chem Res* 58(47):21476–21484. <https://doi.org/10.1021/acs.iecr.9b04285>
- [22] Chatham CA, Zawaski CE, Bobbitt DC, Moore RB, Long TE, Williams CB (2019) Semi-crystalline polymer blends for material extrusion additive manufacturing printability: a case study with poly(ethylene terephthalate) and polypropylene. *Macromol Mater Eng* 304(5):1800764 (11 pages). <https://doi.org/10.1002/mame.201800764>
- [23] Sodeifian G, Ghaseminejad S, Yousefi AA (2019) Preparation of polypropylene/short glass fiber composite as fused deposition modeling (FDM) filament. *Results Phys* 12:205–222. <https://doi.org/10.1016/j.rinp.2018.11.065>
- [24] Carneiro OS, Silva AF, Gomes R (2015) Fused deposition modeling with polypropylene. *Mater Des* 83:768–776. <https://doi.org/10.1016/j.matdes.2015.06.053>
- [25] Banerjee SS, Burbine S, Shivaprakash NK, Mead J (2019) 3D-printable PP/SEBS thermoplastic elastomeric blends: preparation and properties. *Polymers* 11(2):11020347 (13 pages). <https://doi.org/10.3390/polym11020347>

- [26] Spoerk M, Arbeiter F, Raguz I, Weingrill G, Fischinger T, Traxler G, Schuschnigg S, Cardon L, Holzer C (2018) polypropylene filled with glass spheres in extrusion-based additive manufacturing: effect of filler size and printing chamber temperature. *Macromol Mater Eng* 303(7):1800179 (15 pages). <https://doi.org/10.1002/mame.201800179>
- [27] Spoerk M, Sapkota J, Weingrill G, Fischinger T, Arbeiter F, Holzer C (2017) Shrinkage and warpage optimization of expanded-perlite-filled polypropylene composites in extrusion-based additive manufacturing. *Macromol Mater Eng* 302(10):1700143 (13 pages). <https://doi.org/10.1002/mame.201700143>
- [28] Jin M, Neuber C, Schmidt H-W (2020) Tailoring polypropylene for extrusion-based additive manufacturing. *Addit Manuf* 33:101101. <https://doi.org/10.1016/j.addma.2020.101101>
- [29] Das A, Marnot AEC, Fallon JJ, Martin SM, Joseph EG, Bortner MJ (2020) Material extrusion-based additive manufacturing with blends of polypropylene and hydrocarbon resins. *ACS Appl Polym Mater* 2(2):911–921. <https://doi.org/10.1021/acsapm.9b01127>
- [30] Gudadhe A, Bachhar N, Kumar A, Andrade P, Kumaraswamy G (2019) Three-Dimensional Printing with Waste High-Density Polyethylene. *ACS Appl Polym Mater* 1(11):3157–3164. <https://doi.org/10.1021/acsapm.9b00813>
- [31] Peng F, Jiang HW, Woods A, Joo P, Amis EJ, Zacharia NS, Vogt BD (2019) 3D printing with core-shell filaments containing high or low density polyethylene shells. *ACS Appl Polym Mater* 1(2):275–285. <https://doi.org/10.1021/acsapm.8b00186>
- [32] Schirmeister CG, Hees T, Licht EH, Mulhaupt R (2019) 3D printing of high density polyethylene by fused filament fabrication. *Addit Manuf* 28:152–159. <https://doi.org/10.1016/j.addma.2019.05.003>
- [33] Lin JH, Pan YJ, Liu CF, Huang CL, Hsieh CT, Chen CK, Lin ZI, Lou CW (2015) Preparation and compatibility evaluation of polypropylene/high density polyethylene polyblends. *Materials* 8(12):8850–8859. <https://doi.org/10.3390/ma8125496>
- [34] Lotz B, Wittmann JC (1987) Polyethylene isotactic polypropylene epitaxy—analysis of the diffraction patterns of oriented biphasic blends. *J Polym Sci Part B Polym Phys* 25(5):1079–1087. <https://doi.org/10.1002/polb.1987.090250509>
- [35] Gross B, Peterman J (1984) Synergisms of mechanical-properties in blends of semi-crystalline polymers. *J Mater Sci* 19(1):105–112. <https://doi.org/10.1007/BF00552998>
- [36] Gu X, Wang Y, Jiang Y, Liu M, Fu Q, Zhang J (2019) High impact performance induced by a synergistic effect of heteroepitaxy and oriented layer-unoriented layer alternated structure in iPP/HDPE injection molded part. *Polymer* 175:206–214. <https://doi.org/10.1016/j.polymer.2019.05.018>
- [37] Zhou M, Mi D, Hou F, Zhang J (2017) Insight into understanding the evolution of the epitaxy crystallization in isotactic polypropylene and polyethylene blends. *Polym Adv Technol* 28(12):1750–1758. <https://doi.org/10.1002/pat.4052>
- [38] Zhou M, Mi D, Hou F, Zhang J (2017) Tailored crystalline structure and mechanical properties of isotactic polypropylene/high molecular weight polyethylene blend. *Ind Eng Chem Res* 56(29):8385–8392. <https://doi.org/10.1021/acs.iecr.7b01733>
- [39] Su R, Wang K, Zhang Q, Chen F, Fu Q, Hu N, Chen E (2011) Epitaxial crystallization and oriented structure of linear low-density polyethylene/isotactic polypropylene blends obtained via dynamic packing injection molding. *Polym Adv Technol* 22(2):225–231. <https://doi.org/10.1002/pat.1522>
- [40] Na B, Zhang Q, Wang K, Li LB, Fu Q (2005) Origin of various lamellar orientations in high-density polyethylene/isotactic polypropylene blends achieved via dynamic packing injection molding: bulk crystallization versus epitaxy. *Polymer* 46(3):819–825. <https://doi.org/10.1016/j.polymer.2004.11.110>
- [41] Na B, Wang K, Zhao P, Zhang Q, Du RN, Fu Q, Yu ZQ, Chen EQ (2005) Epitaxy growth and directed crystallization of high-density polyethylene in the oriented blends with isotactic polypropylene. *Polymer* 46(14):5258–5267. <https://doi.org/10.1016/j.polymer.2005.04.052>
- [42] Deng P, Whiteside B, Wang F, Norris K, Zhang J (2014) Epitaxial growth and morphological characteristics of isotactic polypropylene/polyethylene blends: Scale effect and mold temperature. *Polym Test* 34:192–201. <https://doi.org/10.1016/j.polymertesting.2014.01.006>
- [43] Turnerjones A, Cobbold AJ (1968) Beta crystalline form of isotactic polypropylene. *J Polym Sci Part B Polym Lett* 6(8PB):539. <https://doi.org/10.1002/pol.1968.110060802>
- [44] Picken SJ, Aerts J, Visser R, Northolt MG (1990) Structure and rheology of aramid solutions—X-ray-scattering measurements. *Macromolecules* 23(16):3849–3854. <https://doi.org/10.1021/ma00218a021>
- [45] Liu H, Chen F, Liu B, Estep G, Zhang J (2010) Super toughened poly(lactic acid) ternary blends by simultaneous dynamic vulcanization and interfacial compatibilization. *Macromolecules* 43(14):6058–6066. <https://doi.org/10.1021/ma101108g>
- [46] Liu M, Hong R, Gu X, Fu Q, Zhang J (2019) Remarkably improved impact fracture toughness of isotactic polypropylene via combining the effects of shear layer-spherulites layer alternated structure and thermal annealing. *Ind Eng*

- Chem Res 58(32):15069–15078. <https://doi.org/10.1021/acs.iecr.9b02858>
- [47] Liu KJ, Zhang J, Liu H, Qian XY, Zhang Y, Wang T, Shen KZ (2013) A multi-layer bioinspired design with evolution of shish-kebab structures induced by controlled periodical shear field. *Express Polym Lett* 7(4):355–364. <https://doi.org/10.3144/expresspolymlett.2013.32>
- [48] van Erp TB, Balzano L, Spoelstra AB, Govaert LE, Peters GWM (2012) Quantification of non-isothermal, multi-phase crystallization of isotactic polypropylene: the influence of shear and pressure. *Polymer* 53(25):5896–5908. <https://doi.org/10.1016/j.polymer.2012.10.027>
- [49] Shmueli Y, Lin Y-C, Lee S, Zhernenkov M, Tannenbaum R, Marom G, Rafailovich MH (2019) In situ time-resolved X-ray scattering study of isotactic polypropylene in additive manufacturing. *ACS Appl Mater Interfaces* 11(40):37112–37120. <https://doi.org/10.1021/acsami.9b12908>
- [50] Gu X, Zhou M, Wang Y, Zhang J (2019) Influence of annealing on the morphology and mechanical properties of iPP/HDPE blend with tailored oriented crystalline structures. *J Polym Res* 26(8):194 (11 pages). <https://doi.org/10.1007/s10965-019-1864-8>
- [51] Lovinger AJ, Williams ML (1980) Tensile properties and morphology of blends of polyethylene and polypropylene. *J Appl Polym Sci* 25(8):1703–1713. <https://doi.org/10.1002/app.1980.070250817>
- [52] Jiang Y, Wu J, Leng J, Cardon L, Zhang J (2019) Reinforced and toughened PP/PS composites prepared by fused filament fabrication (FFF) with in-situ microfibril and shish-kebab structure. *Polymer* 186:121971 (8 pages). <https://doi.org/10.1016/j.polymer.2019.121971>
- [53] Shmueli Y, Jiang J, Zhou Y, Xue Y, Chang C-C, Yuan G, Satija SK, Lee S, Nam C-Y, Kim T, Marom G, Gersappe D, Rafailovich MH (2019) Simultaneous in situ X-ray scattering and infrared imaging of polymer extrusion in additive manufacturing. *ACS Appl Polym Mater* 1(6):1559–1567. <https://doi.org/10.1021/acsapm.9b00328>
- [54] McIlroy C, Graham RS (2018) Modelling flow-enhanced crystallisation during fused filament fabrication of semi-crystalline polymer melts. *Addit Manuf* 24:323–340. <https://doi.org/10.1016/j.addma.2018.10.018>
- [55] Nogales A, Gutierrez-Fernandez E, Garcia-Gutierrez M-C, Ezquerro TA, Rebolgar E, Sics I, Malfois M, Gaidukovs S, Gecis E, Celms K, Bakradze G (2019) Structure development in polymers during fused filament fabrication (FFF): an in situ small- and wide-angle X-ray scattering study using synchrotron radiation. *Macromolecules* 52(24):9715–9723. <https://doi.org/10.1021/acs.macromol.9b01620>

**Publisher's Note** Springer Nature remains neutral with regard to jurisdictional claims in published maps and institutional affiliations.